

Automatic Segmentation of Mammary Tissue using Computer Simulations of Breast Phantoms and Deep-learning Techniques

Lucca R. Peregrino¹, Jordy V. Gomes¹, Thaís G. do Rêgo¹, Yuri de A. M. Barbosa¹,
Telmo de M. e Silva Filho², Andrew D. A. Maidment³ and Bruno Barufaldi^{3,*}

¹Center of Informatics, Federal University of Paraíba, João Pessoa, Brazil

²Department of Statistics, Federal University of Paraíba, João Pessoa, Brazil

³Department of Radiology, University of Pennsylvania, 3640 Hamilton Walk, Philadelphia PA, U.S.A.

Keywords: Phantoms, Tomosynthesis, Deep Learning, U-Net, Segmentation.

Abstract: Digital breast tomosynthesis (DBT) has rapidly emerged for screening mammography to improve cancer detection. Segmentation of dense tissue plays an important role in breast imaging applications to estimate cancer risk. However, the current segmentation methods do not guarantee an ideal ground-truth in clinical practice. Computer simulations provide ground-truth that enables the development of convolutional neural network (CNN) applications designed for image segmentation. This study aims to train a CNN model to segment dense tissue in DBT images simulated using anthropomorphic phantoms. The phantom images were simulated based on clinical settings of a DBT system. A U-Net, a CNN model, was trained with 2,880 images using a slice-wise approach. The U-Net performance was evaluated in terms of percent of density in the central slice and volumetric breast density in the medio-lateral slices. Our results show that the U-Net can segment dense tissue from DBT images with overall loss, accuracy, and intersection over union of 0.27, 0.93, and 0.62 in the central slices, and 0.32, 0.92, and 0.54 in the medio-lateral slices, respectively. These preliminary results allow us to explore the use of CNN architectures to segment dense tissue in clinical images, which is a highly complex task in screening with DBT.

1 INTRODUCTION

Digital mammography (DM) and digital breast tomosynthesis (DBT) are considered the “gold standard” of care for breast cancer screening (Tice and Feldman, 2008; Vedantham et al., 2015; Azar and El-Said, 2013). These imaging modalities increase the sensitivity in cancer detection and reduce the number of recall rates when compared to the traditional screening with screen-film (Vedantham et al., 2015).

Complementary tools such as computer-aided diagnosis systems and convolution neural network (CNN) applications can facilitate the early cancer location by enhancing and detecting lesions (Cheng et al., 2006; Azar and El-Said, 2013), which potentially improve the diagnosis on mammography exams.

Anthropomorphic breast phantoms have been widely used for research and development of mam-

mography imaging systems (Caldwell and Yaffe, 1990; Carton et al., 2011). These phantoms simulate the mammary tissue accurately in terms of size, volume, and composition. Simulations of breast phantoms can be used as data augmentation to support CNN architectures (Lashgari et al., 2020), assisting the lack of data from specific populations (Barufaldi et al., 2018a). In addition, these simulations provide ground-truth images (i.e., ideal reference), which is not provided in clinical practice (Tunçay and Akduman, 2014).

Manual or semi-automatic methods have been developed to obtain ground-truth from images by segmenting and thresholding different findings (Rui et al., 2018; Chatfield et al., 2014; Valverde et al., 2017). In medical imaging, these segmentation methods are commonly performed by experts in radiology. Because of the subjectivity of inter-and/or intra-readers, the output resulting from these methods may include variability and inaccuracy (Oliveira, 2017), while computer simulations provide the *actual ground-truth* for the segmented image.

^a  <https://orcid.org/0000-0002-7779-0288>

^b  <https://orcid.org/0000-0003-0826-6885>

^c  <https://orcid.org/0000-0003-3954-3611>

The large variability of data with ground-truth provided by computer simulations can improve the performance of image segmentation with CNNs (Hamarneh and Jassi, 2010; Li et al., 2009). The ground-truth identifies each breast tissue, structures, and findings to be used as labels for the input images required in CNNs (Hamarneh and Jassi, 2010).

This study aims to develop a CNN model for tissue segmentation using computer simulations of breast phantoms. The CNN model is trained and tested using an U-Net architecture (Ronneberger et al., 2015). Projections are simulated using the acquisition geometry of a clinical DBT system. DBT phantom images are reconstructed using a customized increment between reconstructed slices (0.1 mm). The U-Net architecture is trained using a slice-wise approach to segment glandular tissue from 2,880 DBT reconstructed images.

2 BACKGROUND

2.1 Antropomorphic Breast Phantoms

Anthropomorphic breast phantoms have been widely used to conduct *in-silico* trials (Bakic et al., 2018; Maidment, 2014; Abadi et al., 2020). Breast characteristics such as shape, size, volume, and tissue composition should be accurately simulated in accordance with the human anatomy (Tunçay and Akduman, 2014). In addition, breast anatomical features (e.g., glandular segments, Cooper's ligaments and blood vessels) should be realistically simulated (Elangovan et al., 2017).

To ensure that images simulated using anthropomorphic breast phantoms are comparable to clinical mammograms, validation methods that rely on human visual inspection and/or computer analyses are required. For example, Elangovan *et al.* (2017) propose a method that can rapidly produce a multiplicity of different breast appearance models using 4-alternative forced choice (4-AFC). Using 4-AFCs, they have shown that simulated and real images were statistically indistinguishable by expert breast readers.

However, the recruitment of breast experts needed to validate anthropomorphic phantoms can be a challenging task, and *in-silico* trials have been designed as attempt to simulate human readings. Badano *et al.* (2018) and Bakic *et al.* have reproduced reading interpretations reported on large scale clinical trials designed for pre-market approval of novel imaging technologies (Badano et al., 2018; Bakic et al., 2018). These previous publications reported a successful use

of mathematical models to simulate virtual readers and design virtual anthropomorphic phantoms.

In breast imaging, computer simulations usually require the use of breast phantoms (Bakic et al., 2018; Maidment, 2014; Abadi et al., 2020). In this study, computer simulations of breast phantoms were used to design a novel CNN application for image segmentation using an U-Net architecture.

2.2 U-Net Architecture

CNNs are often used for image classification and segmentation (Rui et al., 2018; Chatfield et al., 2014; Valverde et al., 2017). The U-Net architecture is a CNN that was developed for biomedical image segmentation (Ronneberger et al., 2015). The ultimate goal of the U-Net architecture (Figure 1) is the segmentation and localization of desired objects/structures highlighted in the input images (Paul, 2018). The major benefit of the U-Net is that there is no need to use a large number of images for training and testing (Ronneberger et al., 2015). Thus, U-Net can be useful for segmentation of medical images, due to the fact that the segmented ground-truth is not available in clinical practice. Besides that, U-Net uses a reduced amount of training parameters compared to other CNN's, such as SegNet (Badrinarayanan et al., 2017).

The U-Net architecture consists of contraction (encoder) and expansion (decoder) paths. A set of two convolutions (3×3 kernel) and one maxpooling (2×2 kernel) with ReLU activation are performed in each encoder layer. Similarly, each decoder layer starts with an upsampling and a 2×2 convolution, followed by two 3×3 convolutions with ReLU activation. The encoder provides filtered information (feature maps) acquired during the contraction path to be interpreted by the decoder. The decoder concatenates the output of transposed convolution layers with the feature maps acquired from the encoder at each layer. Finally, an activation function is used to predict classes of the input images based on previous knowledge (training phase) obtained from ground-truth images (Academy, 2019).

The U-Net architecture has been used in several medical applications (Norman et al., 2018; Sevastopolsky, 2017). For example, Tong *et al.* (2018) developed an improved U-Net architecture to segment pulmonary nodules from CT images. The authors concluded that the accuracy of nodule segmentation is comparable or superior to the manual segmentation. A different U-Net application, developed by Norman *et al.* (2018), has shown an improved segmentation of cartilage and meniscus from knees using clinical MRI

images. Similarly, the precision of the automatic segmentation demonstrated to be comparable to the manual segmentation of experts.

In breast imaging, Zhang *et al.* (2020) developed a transfer learning application that uses U-Net and Seg-Net architectures to segment whole-breasts from MRI scans. The authors modified and adapted both architectures using slice-wise approaches and obtained average dice coefficient results of 0.87 (independent test data set). Although the authors presented compelling results, they emphasized that recruiting experts was challenging because of the limited and expensive time from radiologists to manually segment breasts from MRI scans. In addition, the authors could not obtain the manual segmentation (ground-truth) of the entire image dataset.

Several software have been developed to segment breast glandular tissue and estimate volumetric breast density or breast dense area, such as Volpara *et al.* (2014) and LIBRA *et al.* (2012). These software use image processing techniques (e.g., edge detection, support-vector machine, etc.) to segment breast tissue in clinical images, unlike the methods proposed in the current study.

Our proposed method is based on computer simulations that do not require manual segmentation of breast tissue.

3 MATERIALS AND METHODS

3.1 Computer Simulations

The OpenVCT framework (Barufaldi *et al.*, 2018b) was used to simulate anthropomorphic breast phantoms (Zhang *et al.*, 2008; Pokrajac *et al.*, 2012). The breast phantoms are composed by voxel-materials (labels) that represent various tissue types and air (Barufaldi *et al.*, 2018a). The tissue types are simulated using an octree-based recursive partitioning method (Pokrajac *et al.*, 2012). In this method, seed points are randomly selected within the phantom interior and used to simulate glandular and adipose tissue bounded by fibrous Cooper’s ligaments (Figure 2). These tissue types are simulated to mimic the breast anatomy.

We combined and simulated all phantom parameters described in Table 1 (n=96). These parameters were selected based on previous publications (Bakic *et al.*, 2018; Barufaldi *et al.*, 2019). Finally, a breast tissue compression was simulated using a GPU-accelerated mesh software (Barufaldi *et al.*, 2018a). The compression was performed using a medio-lateral (ML) view.

Table 1: Summary of the breast phantom parameters.

Anthropomorphic Breast Phantoms	Parameters
Number of Phantoms (#)	96
Distribution of dense compartments (%)	{1.0; 15.0; 25.0; 50.0}
Breast volume (mL)	700
Breast thickness (mm)	63.3
Voxel size (mm)	{0.1; 0.2}
Number of compartments (#)	{425; 850; 1275; 1700}
Compartment shape	{(0.1; 1.0; 1.0; 2.0), (0.01; 1.0; 1.0; 4.0)}
Ligament thickness (mm)	[0.1;0.18]

The 3D breast phantoms were “sliced” through the entire volume in the sagittal orientation (Figure 2, left). In total, 633 2D slices (784×2053 pixels) were acquired per phantom (ML view). The phantom slices contain label maps at each 0.1 mm thick of compressed breast (Figure 2, right). Each label represents a different x-ray mass attenuation (Hubbell and Seltzer, 1995) used to simulate DBT projections (Feng and Sechopoulos, 2012). For each phantom, a set of 15 x-ray projections was simulated using the acquisition geometry of a clinical DBT system (Table 2). The x-ray projections were simulated using a GPU-enabled x-ray tracing algorithm (Siddon, 1985). The exposure acquisition settings follow the automatic exposure control from the DBT system (Feng and Sechopoulos, 2012).

Table 2: Summary of the DBT acquisition parameters.

DBT System (model)	Selenia Dimensions
X-Ray Imaging	
Anode Material	Tungsten
Filter Material	Aluminum
Filter Thickness (mm)	0.7
Angular Range (°)	[±7.5,±15,±25]
Number of Projections (#)	15
Tube Motion	Continuous
Detector	
Detection Material	a-Se
Detector Element Size(mm)	0.140 × 0.140
Number of Elements (#)	2048 × 1664
Detector Size (mm)	286.72 × 232.96
Source-Image Dis.(mm)	700.0
Rec. Voxel Size (mm)	0.1

A commercial reconstruction software (Briona Std., Real-Time Tomography, Vilanova PA) was used to reconstruct and to process each set of DBT projections (Chui *et al.*, 2012). This software allows us to reconstruct DBT images using customized reconstruction voxel size. In this study, the DBT images

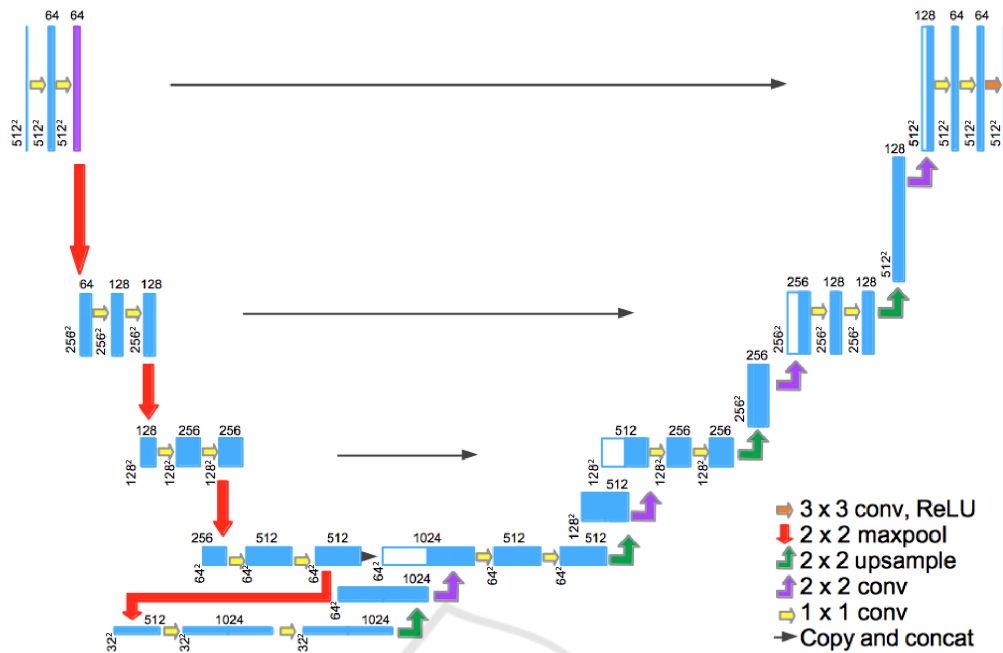


Figure 1: U-Net architecture used in this study. This architecture shows the "u" structure resulting from the encoder and decoder paths.

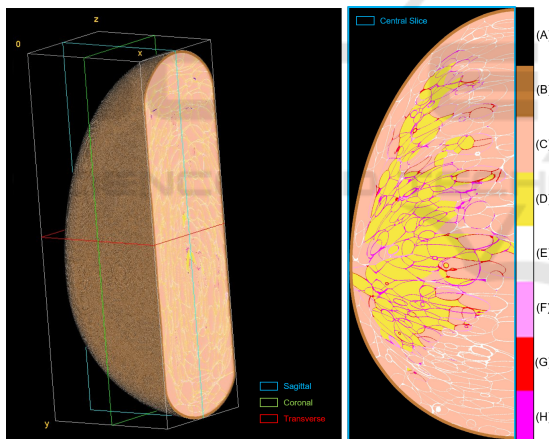


Figure 2: (Left) Volume view of compressed anthropomorphic breast phantom and (right) central slice (ML breast view). The colormap represents the labels used to identify each voxel-material: (A) air, (B) skin, (C) adipose, (D) glandular, (E-H) Cooper's ligaments.

were reconstructed using 0.1 mm increments in depth. In total, 633 reconstructed DBT images (1664×2048 pixels) were acquired per phantom.

3.2 Pre-processing Images

The reconstructed DBT images and correspondent label maps (ground-truth) were used as input for the training and test stages of the U-Net architecture. However, differences between the dimensions of the

input images will result in an ineffective CNN model. Pre-processing techniques were required to match the ground-truth to the respective reconstructed DBT image.

The acquisition geometry (Table 2) was used to locate each label on the ground-truth and the respective pixel value in the DBT image. Next, a cropping operation was applied to each DBT image to eliminate excessive background information from the DBT images (Figure 3, left and middle). Finally, the glandular tissue label was thresholded and segmented from the ground-truth to obtain binary masks used for training the CNN model (Figure 3, right). After these pre-processing steps, the reconstructed DBT image, label map, and binary mask are matched ($778 \times 2,036$ pixels). Finally, both input images, DBT reconstructed image and binary mask, were normalized using the maximum value in bits (2^{14} and 2^8 , respectively), resulting in images with pixel values in a $[0, 1]$ interval. The input images were resized to 512×512 pixels to optimize the CNN model and reduce computational burden.

3.3 Training the Model

To train the segmentation model, we modified the original U-Net parameters (Zhixuhao, 2016; Ronneberger et al., 2015) using the programming language Python. The optimization of the U-Net parameters, as well as training and testing were performed

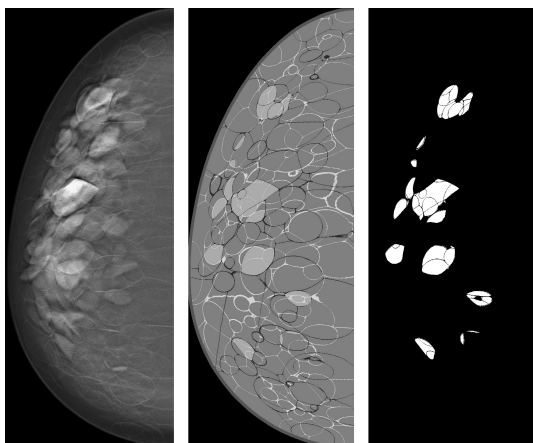


Figure 3: (Left) central slice of reconstructed DBT image, (middle) label map, and (right) binary mask after matching and cropping operations.

using a workstation equipped with Intel(R) Xeon(R) CPU, 16GB RAM, and single graphics card NVIDIA Quadro P5000.

In total, 45 pairs of images (reconstructed DBT image and mask) acquired from 64 phantoms ($n=2,880$ pairs) were used to train the U-Net model. The image pairs were selected using 45 pairs of phantom central slices, which contain regions with the most amount of glandular tissue.

Our U-Net model (Figure 1) was trained using 120 epochs, batch size 4, and image size 512×512 . The weights of the training model were updated after each iteration ($n=720$). These parameters were selected and constrained based on memory used to train the architecture models. The number of epochs was optimized based on loss and accuracy. It is important to mention that the training models are saved every epoch. The training model did not improve significantly after 120 epoch.

3.4 Evaluation Metrics

The binary crossentropy, accuracy, and intersection over union were used to evaluate the performance of the segmentation models. These metrics are defined as:

Binary Crossentropy (Loss) is a loss function that calculates the difference between predicted labels (\hat{y}) and true labels (y). The loss is computed following Equation (1):

$$Loss(y, \hat{y}) = -(y \cdot \log(\hat{y}) + (1 - y) \cdot \log(1 - \hat{y})) \quad (1)$$

Accuracy (Acc) is a metric commonly used for predictive models, calculating the proportion of correct predictions (CP) over the total instances. In our approach, each pixel is an instance ($Total$). The for-

malism of accuracy is defined in accordance with Equation (2):

$$Acc = \frac{CP}{Total} \quad (2)$$

Intersection over Union (IoU) is a metric that computes the segmented area (\hat{y}) that corresponds to the area of the mask (y), dividing what is in common between them (intersection) by the whole (union). Equation (3) shows the IoU calculation:

$$IoU = \frac{area(\hat{y}) \cap area(y)}{area(\hat{y}) \cup area(y)} \quad (3)$$

Pearson's correlation coefficient (ρ) was calculated to evaluate the linear correlation between the evaluated metrics and the percentage of glandular tissue (PD%) in the phantom images. PD% is calculated by using the ratio of glandular labels and non-air labels (e.g., Figure 2).

The observed values were categorized by slice position through the phantom volume and volumetric breast density (VBD).

4 EXPERIMENTAL ANALYSES

Two experiments were performed to test our segmentation model. For both experiments, we used 32 unique breast phantoms. For each experiment, we varied the slice location as input images. Similarly to the training stage, only the central slice images were used as input for the first experiment. For the second experiment, the entire phantom volume divided in slices was used as input images. The phantom slices and DBT reconstructed images close to the phantom skin (about 1 cm in each extremity) were excluded from the experimental analyses due to the lack of glandular tissue for segmentation.

4.1 Using Central Slices

The experiment using only the central slices resulted in a mean Loss, Acc and IoU of 0.27, 0.93, and 0.62, respectively. Figures 4-6 show three examples from our model segmentation using input images that contain regions with different amounts of glandular tissue (i.e., PD%). Note that the accuracy of the U-Net segmentation varies with PD%.

The correlations between PD% and Loss, Acc, and IoU were $\rho=0.77$, $\rho=-0.85$, and $\rho=0.60$, respectively. This correlation analysis shows moderate to high positive correlation between PD%, IoU and Loss, and high negative correlation with Acc. That

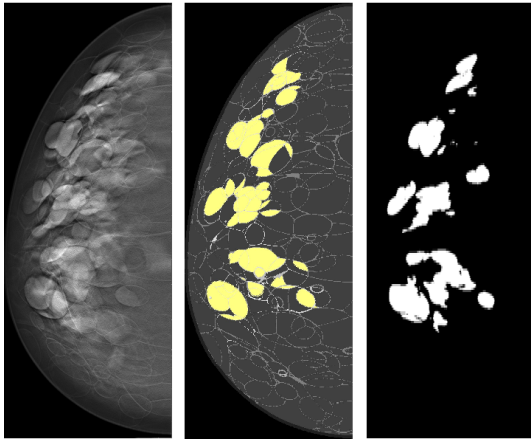


Figure 4: (Left) central slice of reconstructed DBT image, (middle) label map with glandular tissue highlighted in yellow (PD%=12%), and (right) binary segmentation. The segmentation metrics for this input image were 0.18, 0.95, and 0.56 for Loss, Acc, and IoU, respectively.

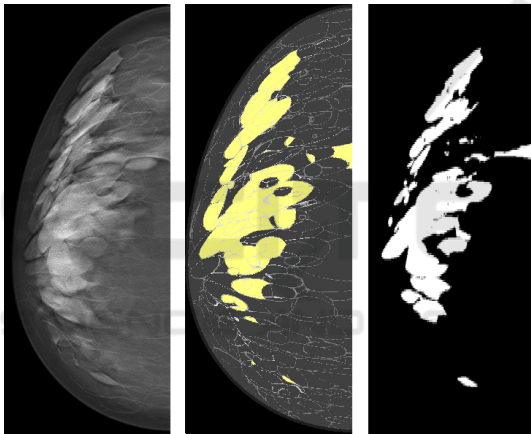


Figure 5: (Left) central slice of reconstructed DBT image, (middle) label map with glandular tissue highlighted in yellow (PD%=20%), and (right) binary segmentation. The segmentation metrics for this input image were 0.19, 0.94, and 0.63 for Loss, Acc, and IoU, respectively.

said, these preliminary results indicate that the accuracy of the U-Net segmentation reduces significantly with PD% (p -value<0.001).

4.2 Using Medio-lateral Slices

We also evaluated the U-Net segmentation using all phantom slices that contain glandular labels (ML slices). In total, over 480 ML slices per phantom were selected for this experiment. The U-Net segmentation resulted in overall performance with mean Loss, Acc, and IoU of 0.32, 0.92, and 0.54, respectively (Figure 7a). Note that there was a slight reduction in the Acc and IoU metrics compared to the previous experiment.

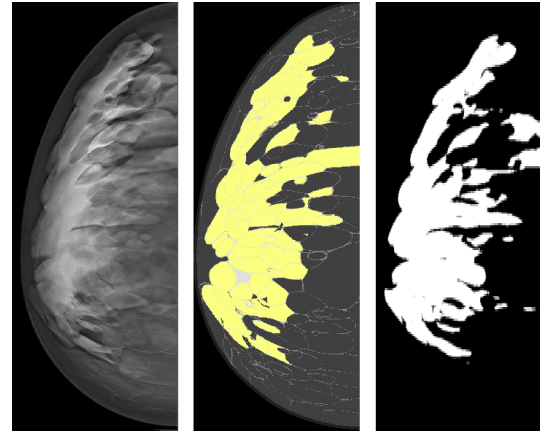


Figure 6: (Left) central slice of reconstructed DBT image, (middle) label map with glandular tissue highlighted in yellow (PD%=34%), and (right) binary segmentation. The segmentation metrics for this input image were 0.31, 0.91, and 0.70 for Loss, Acc, and IoU, respectively.

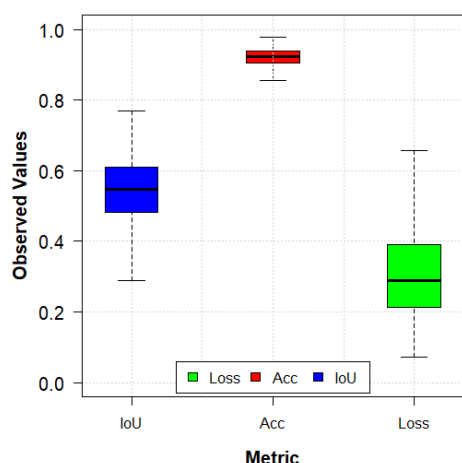
Figure 7b shows the results of the metrics categorized by slice position through the entire phantom volume. The slice position also affects the U-Net performance, since our CNN was trained using only central slices. The relative difference in IoU between slice positions can reach up to 20%. These differences can also be seen in the Loss. However, these are preliminary results and a more detailed statistical analysis is required to evaluate the U-Net performance in depth.

Finally, Figure 7c shows the Acc results categorized by VBD. These boxplots show changes in U-Net performance throughout the glandular volume of breast phantoms. Note that the overall U-Net performance tends to reduce with denser phantoms (i.e., higher VBD). Again, these are preliminary results and a more detailed statistical analysis is required to support this observation.

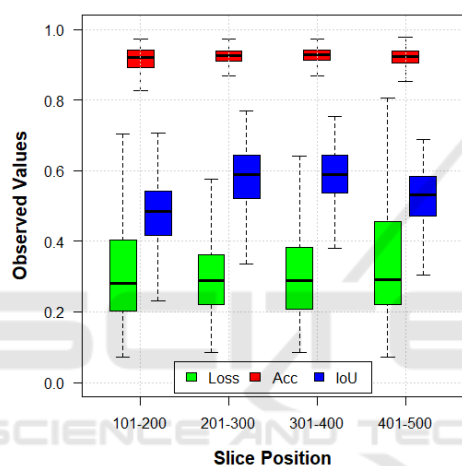
5 CONCLUSIONS

These preliminary results show that our U-Net implementation can segment glandular tissue from DBT images with high accuracy. The computer simulations are supervised, thus a known ground-truth is available as input images for the U-Net training. Although our results were based on simulations, our U-Net implementation can be potentially extended to clinical applications if a reasonable ground-truth data set is provided.

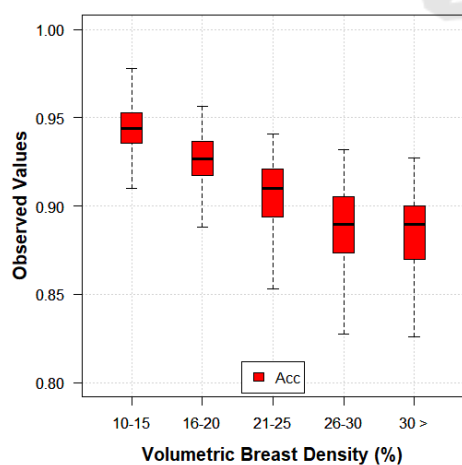
This U-Net application allows us to evaluate the impact of 2D breast parameters (PD%) using particular slices and 3D breast parameters (VBD) using sets of slices as input images. For future work, we will provide a more complete statistical analysis of our



(a)



(b)



(c)

Figure 7: Boxplots of metrics evaluated using reconstructed slices obtained from 10.1-50.0 mm of phantom thickness (0.1 mm increment). (a) Observed values categorized by metrics, (b) as a function of slice position, and (c) as a function of VBD. Note that there is a difference in y-scale in (c), compared to (a) and (b).

dataset and further explore the use of 3D CNNs for volume segmentation.

ACKNOWLEDGEMENTS

Funding for the research is provided by the following grants: BWF IRSA 1016451, DoD W81XWH-18-1-0082, and AAPM 2020 Research Seed Grant.

REFERENCES

Abadi, E., Segars, W. P., Tsui, B. M., Kinahan, P. E., Bottenus, N., Frangi, A. F., Maidment, A., Lo, J., and Samei, E. (2020). Virtual clinical trials in medical imaging: a review. *Journal of Medical Imaging*, 7(4):042805.

Academy, D. S. (2019). Deep learning book.

Azar, A. T. and El-Said, S. A. (2013). Probabilistic neural network for breast cancer classification. *Neural Computing and Applications*, 23(6):1737–1751.

Badano, A., Graff, C. G., Badal, A., Sharma, D., Zeng, R., Samuelson, F. W., Glick, S. J., and Myers, K. J. (2018). Evaluation of digital breast tomosynthesis as replacement of full-field digital mammography using an in silico imaging trial. *JAMA network open*, 1(7):e185474–e185474.

Badrinarayanan, V., Kendall, A., and Cipolla, R. (2017). Segnet: A deep convolutional encoder-decoder architecture for image segmentation. *IEEE transactions on pattern analysis and machine intelligence*, 39(12):2481–2495.

Bakic, P. R., Barufaldi, B., Higginbotham, D., Weinstein, S. P., Avanaki, A. N., Espig, K. S., Xthona, A., Kimpe, T. R. L., and Maidment, A. D. A. (2018). Virtual clinical trial of lesion detection in digital mammography and digital breast tomosynthesis. In Lo, J. Y., Schmidt, T. G., and Chen, G.-H., editors, *Medical Imaging 2018: Physics of Medical Imaging*, volume 10573, pages 30–42. International Society for Optics and Photonics, SPIE.

Barufaldi, B., Bakic, P., and Maidment, A. (2019). Multiple-reader, multiple-case ROC analysis for determining the limit of calcification detection in tomosynthesis. In Schmidt, T. G., Chen, G.-H., and Bosmans, H., editors, *Medical Imaging 2019: Physics of Medical Imaging*, volume 10948, pages 157–163. International Society for Optics and Photonics, SPIE.

Barufaldi, B., Bakic, P. R., Pokrajac, D. D., Lago, M. A., and Maidment, A. D. (2018a). Developing populations of software breast phantoms for virtual clinical trials. In *14th International Workshop on Breast Imaging (IWBI 2018)*, volume 10718, page 107181U. International Society for Optics and Photonics.

Barufaldi, B., Higginbotham, D., Bakic, P. R., and Maidment, A. D. A. (2018b). OpenVCT: a GPU-accelerated virtual clinical trial pipeline for mammography and digital breast tomosynthesis. In Lo, J. Y.,

- Schmidt, T. G., and Chen, G.-H., editors, *Medical Imaging 2018: Physics of Medical Imaging*, volume 10573, pages 1333 – 1340. International Society for Optics and Photonics, SPIE.
- Caldwell, C. B. and Yaffe, M. J. (1990). Development of an anthropomorphic breast phantom. *Medical physics*, 17(2):273–280.
- Carton, A.-K., Bakic, P., Ullberg, C., Derand, H., and Maidment, A. D. (2011). Development of a physical 3d anthropomorphic breast phantom. *Medical physics*, 38(2):891–896.
- Chatfield, K., Simonyan, K., Vedaldi, A., and Zisserman, A. (2014). Return of the devil in the details: Delving deep into convolutional nets. *CoRR*, abs/1405.3531.
- Cheng, H.-D., Shi, X., Min, R., Hu, L., Cai, X., and Du, H. (2006). Approaches for automated detection and classification of masses in mammograms. *Pattern recognition*, 39(4):646–668.
- Chui, J. H., Pokrajac, D. D., Maidment, A. D. A., and Bakic, P. R. (2012). Roadmap for efficient parallelization of breast anatomy simulation. In Pelc, N. J., Nishikawa, R. M., and Whiting, B. R., editors, *Medical Imaging 2012: Physics of Medical Imaging*, volume 8313, pages 1369 – 1378. International Society for Optics and Photonics, SPIE.
- Elangovan, P., Mackenzie, A., Dance, D. R., Young, K. C., Cooke, V., Wilkinson, L., Given-Wilson, R. M., Wallis, M. G., and Wells, K. (2017). Design and validation of realistic breast models for use in multiple alternative forced choice virtual clinical trials. *Physics in Medicine & Biology*, 62(7):2778.
- Feng, S. S. J. and Sechopoulos, I. (2012). Clinical digital breast tomosynthesis system: dosimetric characterization. *Radiology*, 263(1):35–42.
- Hamameh, G. and Jassi, P. (2010). Vascusynth: Simulating vascular trees for generating volumetric image data with ground-truth segmentation and tree analysis. *Computerized medical imaging and graphics*, 34(8):605–616.
- Hubbell, J. H. and Seltzer, S. M. (1995). Tables of x-ray mass attenuation coefficients and mass energy-absorption coefficients 1 keV to 20 MeV for elements Z= 1 to 92 and 48 additional substances of dosimetric interest. Technical report, National Inst. of Standards and Technology-PL, Gaithersburg, MD (United . . .
- Lashgari, E., Liang, D., and Maoz, U. (2020). Data augmentation for deep-learning-based electroencephalography. *Journal of Neuroscience Methods*, page 108885.
- Li, C. M., Segars, W. P., Tourassi, G. D., Boone, J. M., and Dobbins III, J. T. (2009). Methodology for generating a 3d computerized breast phantom from empirical data. *Medical physics*, 36(7):3122–3131.
- Maidment, A. D. (2014). Virtual clinical trials for the assessment of novel breast screening modalities. In *International Workshop on Digital Mammography*, pages 1–8. Springer.
- Norman, B., Pedoia, V., and Majumdar, S. (2018). Use of 2d u-net convolutional neural networks for automated cartilage and meniscus segmentation of knee mr imaging data to determine relaxometry and morphometry. *Radiology*, 288(1):177–185.
- Oliveira, W. d. S. (2017). *Consenso de segmentações de imagens usando classificação de padrões*. PhD thesis, Universidade Federal de Pernambuco.
- Paul, S. (2018). Learn how to train u-net on your dataset. <https://medium.com/coinmonks/learn-how-to-train-u-net-on-your-dataset-8e3f89fbd623>.
- Pokrajac, D. D., Maidment, A. D., and Bakic, P. R. (2012). Optimized generation of high resolution breast anthropomorphic software phantoms. *Medical physics*, 39(4):2290–2302.
- Ronneberger, O., Fischer, P., and Brox, T. (2015). U-net: Convolutional networks for biomedical image segmentation. In *International Conference on Medical image computing and computer-assisted intervention*, pages 234–241. Springer.
- Rui, T., Zou, J., Zhou, Y., Fei, J., and Yang, C. (2018). Convolutional neural network feature maps selection based on l1. *Multimedia Tools and Applications*, 77(9):10635–10649.
- Sevastopolsky, A. (2017). Optic disc and cup segmentation methods for glaucoma detection with modification of u-net convolutional neural network. *Pattern Recognition and Image Analysis*, 27(3):618–624.
- Siddon, R. L. (1985). Fast calculation of the exact radiological path for a three-dimensional ct array. *Medical physics*, 12(2):252–255.
- Tice, J. and Feldman, M. (2008). Full-field digital mammography compared with screen-film mammography in the detection of breast cancer: Rays of light through dmist or more fog? *Breast cancer research and treatment*, 107:157–65.
- Tunçay, A. H. and Akduman, I. (2014). Realistic microwave breast models through t1-weighted 3-d mri data. *IEEE Transactions on Biomedical Engineering*, 62(2):688–698.
- Valverde, S., Cabezas, M., Roura, E., González-Villà, S., Pareto, D., Vilanova, J. C., Ramió-Torrentà, L., Rovira, A., Oliver, A., and Lladó, X. (2017). Improving automated multiple sclerosis lesion segmentation with a cascaded 3d convolutional neural network approach. *CoRR*, abs/1702.04869.
- Vedantham, S., Karellas, A., Vijayaraghavan, G. R., and Kopans, D. B. (2015). Digital breast tomosynthesis: State of the art. *Radiology*, 277(3):663–684. PMID: 26599926.
- Zhang, C., Bakic, P., and Maidment, A. (2008). Development of an anthropomorphic breast software phantom based on region growing algorithm - art. no. 69180v. *Proc SPIE*, 6918.
- Zhixuhao (2016). Implementation of deep learning framework – unet, using keras. <https://github.com/zhixuhao/unet>.